www.springer.com/41230
https://doi.org/10.1007/s41230-026-5154-x
Research & Development
Vol. 23 No. 3 May 2026
CHINA FOUNDRY

Microstructure and mechanical properties of high pressure die casting AE81 magnesium alloy battery module ends

He-cong Xie[1, 2], *Jiang-feng Song[1, 2], Chuang-ming Li[1, 2], Zhi-hua Dong[1, 2], Ang Zhang[1, 2], Jiang Zheng[1, 2], Dao-yan Yang[3], Wei Ren[3], Xian-yue Qin[3], Hong-fen Feng[4], Dong-xia Xiang[5], and **Bin Jiang[1, 2]

1. National Engineering Research Center for Magnesium Alloys, Chongqing University, Chongqing 400044, China

2. State Key Laboratory of Advanced Casting Technologies, Chongqing University, Chongqing 400044, China

3. Chongqing Boao Mg-Al Manufacturing Co., Ltd., Chongqing 400800, China

4. Shanxi Yinguang Huasheng Magnesium Industry Co., Ltd., Yuncheng, Shanxi 043800, China

5. Chongqing Advanced Light Metal Research Institute, Chongqing 400044, China

Abstract: AE81 magnesium alloy castings for electric vehicle battery module ends were fabricated using high pressure die casting (HPDC). Effects of filling behavior and solidification sequence on the spatial distribution of microstructure and mechanical properties were systematically investigated. The results indicate that along the flow path toward the overflow gate, the area fraction of externally solidified crystals (ESCs) gradually decreases, and the average grain size becomes finer, resulting in a slight increase in yield strength. In addition, the pores' volume fraction significantly affects ductility and tensile strength, with the gate region exhibiting the highest porosity (0.74%) and thus the lowest elongation (4.3%) and ultimate tensile strength (218 MPa). In other regions, the porosity decreases to 0.33%–0.39%, resulting in increased elongation (6%–7%) and higher ultimate tensile strength (235–242 MPa). Analysis of the microstructure-property relationship reveals that the yield strength follows the Hall-Petch relationship, while elongation and tensile strength are negatively correlated with pore volume fraction. This finding elucidates the mechanism behind the formation of performance gradients in HPDC magnesium alloys and provides a theoretical basis for the design of lightweight components in new energy vehicles.

Keywords: high pressure die casting; AE81 magnesium alloy; battery module end; microstructure; mechanical properties; pore

CLC numbers: TG146.22 **Document code:** A **Article ID:** 1672-6421(2026)03-291-12

1 Introduction

In response to the twin global challenges of environmental deterioration and energy scarcity, promoting new energy vehicles has become a viable strategy for lowering CO_2 emissions and reducing reliance on fossil fuels[1-4]. Within this context, vehicle lightweighting technology has attracted considerable attention as a key direction for the development of electric vehicles. Magnesium alloys, owing to their low density (only two-thirds that of aluminum and one-quarter that of steel)[5, 6], high specific strength[7], and excellent damping capacity[8], are widely recognized as the most promising lightweight metallic materials. These characteristics endow magnesium alloys with significant engineering value in weight reduction for new energy vehicles[9, 10], especially in the lightweight design of key components such as battery pack structures and vehicle body frames.

High pressure die casting (HPDC) is a key manufacturing technique for magnesium alloy automotive parts, offering an exceptional surface finish and capacity

***Jiang-feng Song**

Ph. D., Professor. Her primary research areas include hot tearing in magnesium alloy casting, edge cracking in magnesium alloy sheet rolling, and the development of die-cast magnesium alloys along with defect control.

E-mail: jiangfeng.song@cqu.edu.cn

****Bin Jiang**

Ph. D., Professor. His main research focuses on novel magnesium alloy materials, new ultra-lightweight magnesium alloys, and the processing of large-scale magnesium alloy components along with sheet and strip.

E-mail: jiangbinrong@cqu.edu.cn

Received: 2025-07-09; Revised: 2025-09-09; Accepted: 2025-11-10

to produce thin-walled, complex geometries[11, 12]. Compared with aluminum alloys, HPDC of magnesium alloys significantly extends die life and improves production efficiency. It has been widely applied in mass production of small to medium-sized structural components such as steering wheels, shock towers, and dashboard brackets, achieving notable energy-saving and emission-reduction benefits[3]. However, commercially available die-cast magnesium alloys are still mainly limited to low-strength AM series (AM50A, AM60B)[13, 14] and AZ series (AZ91D)[15], whose room-temperature mechanical properties are generally low, making them inadequate for structural applications in electric vehicles. To overcome this technical bottleneck, our research team has developed a novel HPDC AE81 magnesium alloy (Mg-8Al-0.7Zn-1.5Ce-0.25Mn-0.25Sb-0.1Sr) through a multi-element microalloying design approach[16]. While maintaining cost competitiveness, this alloy exhibits an excellent combination of mechanical properties, with a room-temperature yield strength (YS) of 190±6.1 MPa, an ultimate tensile strength (UTS) of up to 290±9.8 MPa, and an elongation (EL) of approximately 10%, achieving an optimal balance of strength, ductility, and economy. It offers an ideal lightweight material solution for critical load-bearing components in electric vehicles.

During the HPDC process of automotive thin-walled structural components, the metal melt undergoes complex physical phenomena including slow movement in the shot sleeve, high-speed and high-pressure mold filling, and non-equilibrium solidification[17, 18]. These phenomena inevitably lead to heterogeneity in microstructure and mechanical properties. Niu et al.[19] focused on the microstructural and mechanical characteristics of large-scale thin-walled HPDC aluminum alloy castings with a melt flow length of 1,230 mm. Their results revealed that along the melt flow direction from the gate to the overflow, both the size and fraction of coarse α-Al grains decreased, accompanied by a reduction in average grain size, resulting in a slight increase in yield strength. With increasing melt flow distance, the pore volume fraction significantly increased, which in turn led to a sharp decline in alloy ductility. It has been reported that filling conditions, heat transfer behavior, solidification sequence, and cooling rate within the mold cavity significantly affect the microstructure and mechanical properties of HPDC castings[20-22]. However, there remains a significant gap in the literature concerning the correlation between microstructure and mechanical properties in complex thin-walled HPDC magnesium alloy components. In particular, the coupling mechanism between melt flow patterns and solidification sequence in controlling the spatial distribution of properties has yet to be elucidated. Addressing this scientific issue holds substantial engineering significance for achieving precise control over the performance of large, thin-walled magnesium alloy castings.

X-ray computed tomography (CT), as a non-destructive three-dimensional (3D) characterization method, has evolved into an essential analytical tool for investigating alloy solidification dynamics, spatial distribution of secondary phases, and the evolution of pore defects[23-27]. This technique enables precise quantification of dendritic morphology evolution, volume fraction and size distribution of secondary phases, and pore network connectivity, contributing to significant advances in materials science research[28-30]. It serves as an indispensable tool for uncovering the mechanisms underlying defect formation in HPDC magnesium alloys.

In this study, AE81 magnesium alloy battery module end castings were successfully fabricated using the HPDC process. A comprehensive investigation of the microstructure and properties of the battery module ends was conducted using scanning electron microscopy (SEM), X-ray CT, and finite element modeling. Fundamental characteristics, including defect distribution, mechanical properties, microstructure, and fracture morphology at different casting locations, were evaluated. Finally, the study examined the microstructural heterogeneity induced by melt flow and casting solidification. This provides theoretical guidance for improving the tensile properties of HPDC AE81 magnesium alloy castings.

2 Experimental procedure

The preparation of the HPDC AE81 magnesium alloy battery module end comprised metal melting, pouring, and die casting steps. High-purity Mg (99.9wt.%), Zn (99.9wt.%), Al (99.9wt.%), Sb (99.9wt.%), and master alloys including Mg-10wt.%Mn, Mg-30wt.%Sr, and Mg-30wt.%Ce were used as raw materials according to the designed composition ratio. Pure Mg was firstly heated in a resistance furnace. Upon reaching approximately 500 °C, a protective gas mixture of CO_2 and SF_6 (volume ratio 100:1) was introduced to prevent oxidation. Once the pure Mg was fully melted, the master alloys were gradually added, and the furnace temperature was raised to 740 °C. After complete melting, the alloy melt was refined for 10 min, followed by slag removal. The melt was allowed to cool naturally to 720 °C and held for approximately 15 min before casting. Subsequently, the prepared AE81 melt was poured into a 650 t cold chamber die casting machine (YIZUMI D-M650) to produce the castings shown in Fig. 1(a). The specific die casting parameters are listed in Table 1. Approximately 100 castings were produced during this experimental run. The actual chemical composition of the alloy was determined using an inductively coupled plasma optical emission spectrometer (ICP-Agilent 725OES), and the results are presented in Table 2.

Tensile specimens were sampled from different areas of the battery module end, as shown in Fig. 1(b). Sample 1 was taken from a location close to the gate, while Sample 4 was taken from a location away from the gate. Table 3 provides the thickness and flow length corresponding to various sampling positions. The tensile samples featured a dog-bone shape, with detailed dimensions provided in Fig. 1(c), including a gauge length of 12 mm and a width of 6 mm. Additionally, mechanical properties at room temperature were evaluated at various locations of the HPDC AE81 magnesium alloy casting using an electronic universal testing machine (CMT 6305-300 kN) at a

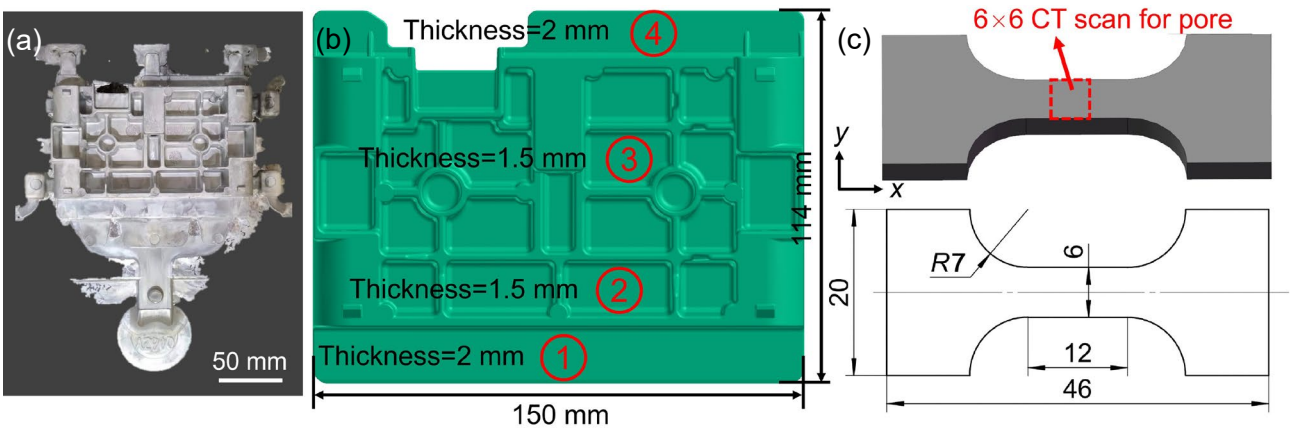

Fig. 1: Battery module end casting (a), room-temperature tensile sampling locations (b), and regions for microstructural analysis and dimensions of room-temperature tensile specimens (unit: mm) (c)

Table 1: Process parameters adopted during HPDC of AE81 magnesium alloy

Slow shot speed ($m \cdot s^{-1}$)	Fast shot speed ($m \cdot s^{-1}$)	Mold temperature (°C)	Melting temperature (°C)	Intensification casting pressure (MPa)
0.15	6	200	720	30

Table 2: Actual chemical composition of AE81 magnesium alloy (wt.%)

Al	Zn	Ce	Mn	Sb	Sr	Mg
8.15	0.74	1.19	0.21	0.16	0.01	Bal.

Table 3: Sample thickness and flow length at different sampling locations

Sample No.	Sample thickness (mm)	Flow length (mm)
1	2.0	135
2	1.5	156
3	1.5	195
4	2.0	233

constant crosshead speed of 1 $mm \cdot min^{-1}$. Triplicate tests were conducted for each sampling location to ensure reproducibility, and the average value was calculated.

The two-dimensional microstructure of the alloy was characterized using a scanning electron microscope (Thermo Scientific Apreo 2S) equipped with a backscattered electron (BSE) detector, energy-dispersive spectroscopy (EDS), and electron backscatter diffraction (EBSD) detectors. The analyzed region corresponded to the red dashed box in Fig. 1(c). For SEM and EBSD analysis, samples were sequentially ground with 600 to 3000 grit abrasive papers followed by mechanical polishing until a mirror-like, scratch-free surface was obtained. Additionally, EBSD specimens were electrolytically polished using an AC_2 solution at –30 °C.

Cuboid specimens measuring 6 mm in length, 6 mm in width, and 1.5–2.0 mm in thickness were extracted from the intact room-temperature tensile sample for X-ray tomography [Fig. 1(c)] to investigate pore distribution. The micro-CT tensile test of HPDC AE81 magnesium alloy was conducted at the Advanced Materials Research Institute, Yangtze Delta. The X-ray microscope (XLAB-2000) operated at 60 kV and 90 μA, achieving a spatial resolution of 5.08 μm. Following CT data acquisition, the 3D pore morphology was reconstructed using Avizo 2022 software. Relevant morphological parameters such as pore diameter, volume, sphericity, and aspect ratio were extracted from the software.

3 Results and discussion

3.1 Microstructure

EBSD maps of various locations in the battery module end are shown in Fig. 2. It can be observed that several coarse grains are surrounded by numerous finer grains, forming a bimodal-like microstructure. During the HPDC, the molten alloy initially contacts the shot sleeve wall, where it undergoes preferential solidification to form coarse dendritic or equiaxed crystals. Subsequently, these coarse grains are transported by the molten flow into the die cavity during the fast shot phase, leading to the formation of externally solidified crystals (ESCs). In order to quantify the distribution characteristics of ESCs, the size threshold for ESCs in HPDC AE81 magnesium alloy was defined as 10 μm in this work. Notably, adjacent ESCs in the microstructure share identical crystallographic orientations but are separated by distinct high-angle grain boundaries, suggesting that they originated from a single ESC that fragmented under high shear stress during rapid mold filling. In contrast, the fine primary α-Mg grains exhibit random orientations and pronounced anisotropy, indicative of rapid nucleation during solidification within the die cavity.

Kernel average misorientation (KAM) is widely employed to characterize the density and distribution of geometrically necessary dislocations (GNDs) in alloys, where GNDs density serves as an indicator of internal stress levels. Typically, a

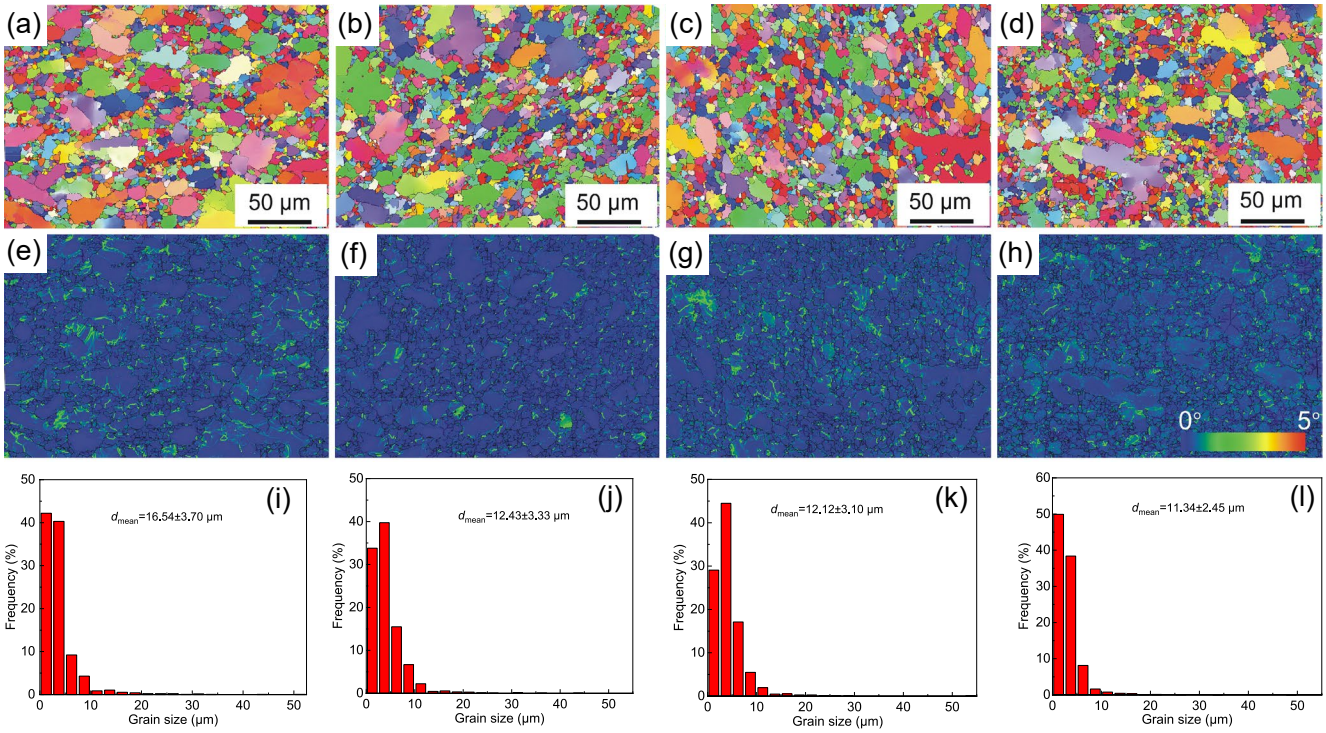

Fig. 2: EBSD microstructures and grain size statistics at different sampling positions: (a), (e), (i) Sample 1; (b), (f), (j) Sample 2; (c), (g), (k) Sample 3; and (d), (h), (l) Sample 4

higher GNDs density correlates with greater localized strain[31]. Notably, numerous low-angle grain boundaries are observed within the coarse grains. KAM maps reveal elevated values near these low-angle grain boundaries, likely due to thermal stresses arising from uneven cooling rates between the surface and core during solidification. These stresses induce localized plastic deformation and subsequent dislocation accumulation, accounting for the increased KAM values. Furthermore, during the HPDC process, high shear stresses may induce plastic deformation of dendrite fragments without causing complete fragmentation or dislocation recovery, contributing to elevated local KAM values in ESCs. Additionally, inverse pole figure (IPF) maps were utilized to quantify grain sizes at various sampling positions [Figs. 2(i–l)], revealing significant variations in average grain size across regions. Specifically, the average grain size in Sample 1 (16.54±3.70 μm) is markedly larger than in Samples 2 (12.43±3.33 μm), 3 (12.12±3.10 μm), and 4 (11.34±2.45 μm).

Figure 3 presents the morphologies of second phases at different sampling positions of the AE81 magnesium alloy battery module end. SEM analysis indicates that the microstructure predominantly consists of an α-Mg equiaxed matrix with multiple intermetallic compounds distributed both within grains and along grain boundaries. Based on morphological features and previous studies, four types of second phases are identified: the gray phase commonly found in Mg alloys is $Mg_{17}Al_{12}$ with a body-centered cubic structure[32]; the bright white blocky phase is $Al_{10}Ce_2Mn_7$, which has a hexagonal crystal system with lattice constants a=0.874 nm and c=1.297 nm[33]; the bright white needle-like phase is $Al_{11}Ce_3$, characterized by a body-centered orthorhombic structure (space group Immm), with lattice constants a=0.44 nm, b=1.30 nm, c=1.01 nm[32]; and the bright white particulate phase is Al_2Ce, which has a face-centered cubic structure with lattice constant a=0.7700 nm[34]. Overall, the morphology and distribution of the second phases exhibit minimal variation across different positions of the AE81 magnesium alloy castings. Additionally, pores are observed in all sampled regions. Detailed characterization of these pores will be discussed in subsequent sections.

3.2 Morphology and distribution of pores

Using X-ray CT and image processing with Avizo 2022 software, the 3D morphology and geometric parameters of pores in HPDC AE81 magnesium alloy can be quantitatively characterized. Pores are often characterized by their volume, equivalent diameter, and sphericity. Among these parameters, sphericity is particularly critical, as it reflects the morphological complexity of the pores. In this study, sphericity (*Sph*) is defined as the ratio of the surface area of the pore to that of an equivalent sphere with the same volume[35], and can be expressed as:

$$Sph = \frac{\pi^{1/3}(6B_v)^{2/3}}{S_v} \quad (1)$$

where, B_v and S_v denote the volume and surface area of the pore, respectively. When the sphericity approaches 1, the pore is considered a near-perfect spherical pore. Based on the pore formation mechanisms and morphological characteristics (volume and sphericity)[14, 36-38], pores can be classified accordingly. Earlier research[34] indicates that pore classification primarily uses two thresholds: a volume of 6.4×10^4 μm^3 (equivalent to a diameter of approximately 50 μm) and a sphericity value of 0.5. Pores are ultimately classified into four types according

to these criteria: (1) Net-shrinkage (diameter>50 μm, sphericity<0.5), caused by extensive ESCs aggregation, which obstructs interdendritic liquid feeding and leads to a large, low-sphericity interconnected pore network [(Fig. 4(c)]; (2) Gas-shrinkage pore (diameter>50 μm, sphericity>0.5), composed of gas pores combined with surrounding shrinkage pores, also of large size [Fig. 4(d)]; (3) Island-shrinkage (diameter<50 μm, sphericity<0.5), formed due to sparse ESCs aggregation and poor feeding between ESCs dendrites, smaller in size [Fig. 4(e)]; (4) Gas pore (diameter<50 μm, sphericity>0.5), arising from gas entrapment during HPDC, showing spherical shapes under interfacial tension, and further compressed by pressure intensification in the late HPDC process, leading to small, rounded pores [Fig. 4(f)]. This classification aligns with the findings of Zhang and Yu et al.[37, 38], revealing from the perspective of formation mechanism the synergistic influence of ESCs distribution and process parameters on defect morphology.

Figure 5 presents the 3D distribution and morphology of pores in HPDC AE81 magnesium alloy castings at different

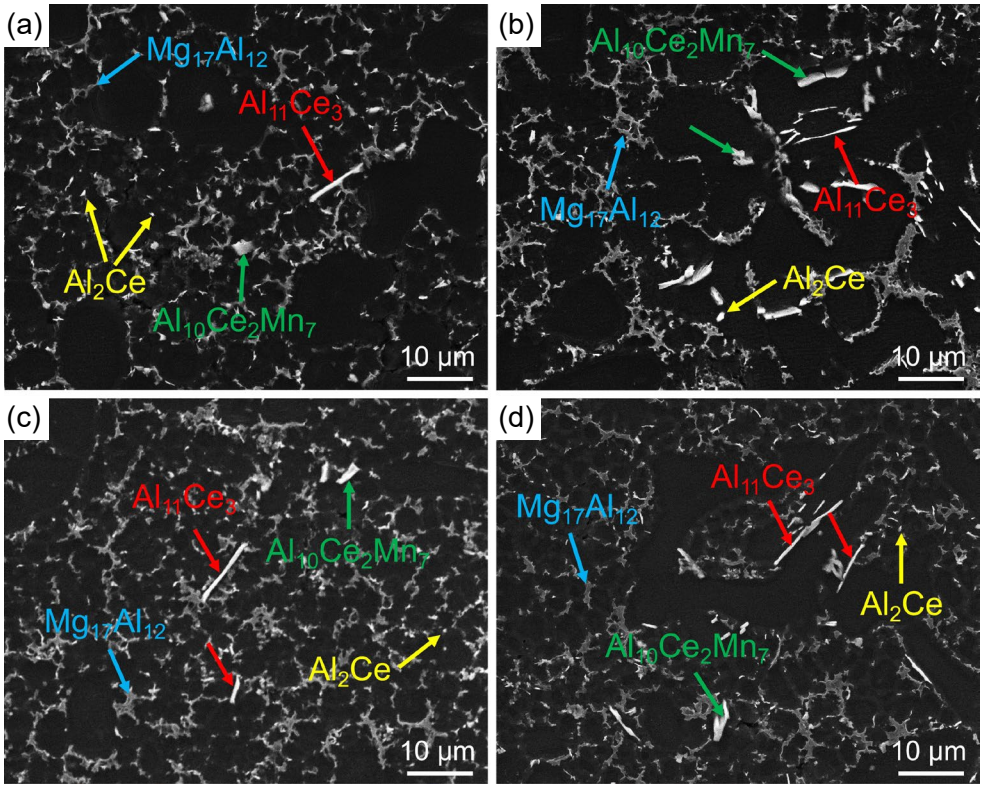

Fig. 3: SEM microstructures at different sampling positions: (a) Sample 1; (b) Sample 2; (c) Sample 3; and (d) Sample 4

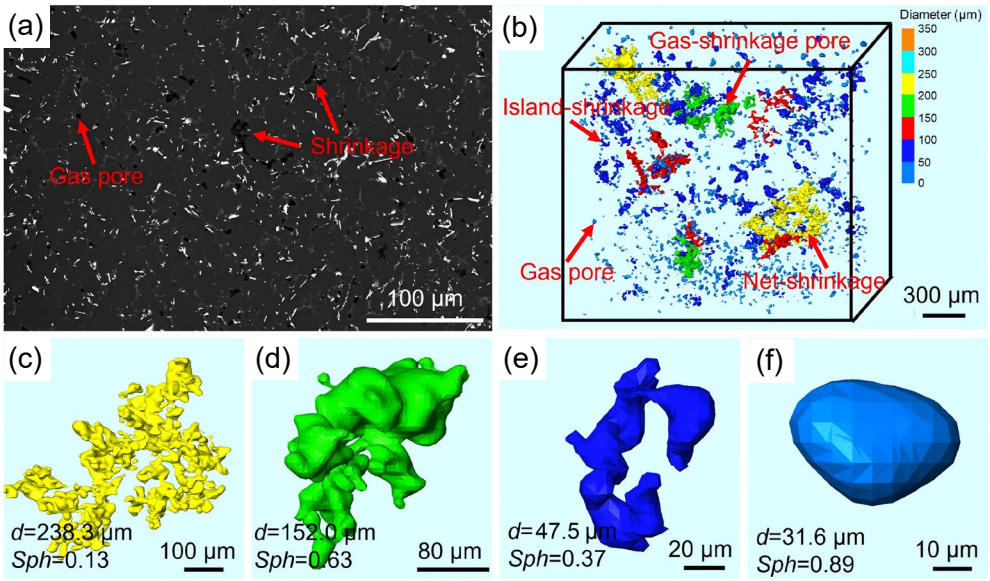

Fig. 4: Typical defects of AE81 magnesium alloy shown by SEM morphology and 3D morphology: (a) SEM microstructure; (b) 3D morphology of pores; (c) net-shrinkage; (d) gas-shrinkage pore; (e) island-shrinkage; (f) gas pore

positions. At Sample 1, the pores predominantly comprise large-scale interconnected networks of shrinkage pores (net-shrinkage), gas-shrinkage pores, island-shrinkage, and gas pores. It is evident that this sample contains numerous morphologically complex and larger networked shrinkage pores, with a clearly discernible defect band visible in the *XZ* plane, as shown in Figs. 5(a) and (e). Sample 2 demonstrates a significant reduction in net-shrinkage compared to Sample 1, and the volume and quantity of pores are also markedly smaller, although the pore distribution remains heterogeneous, with larger pores localized in the upper-left quadrant, while relatively regular pores are clustered in the lower-right quadrant. Samples 3 and 4 exhibit pore morphologies analogous to Sample 2, but the pore distribution is more uniform. Collectively, the 3D reconstruction reveals that the number and size of pores at Samples 2 to 4 are significantly smaller than those at Sample 1. Previous studies have shown that pore morphology and distribution are closely related to mechanical properties, and a higher density of pore defects may lead to deterioration of mechanical properties[13, 39, 40].

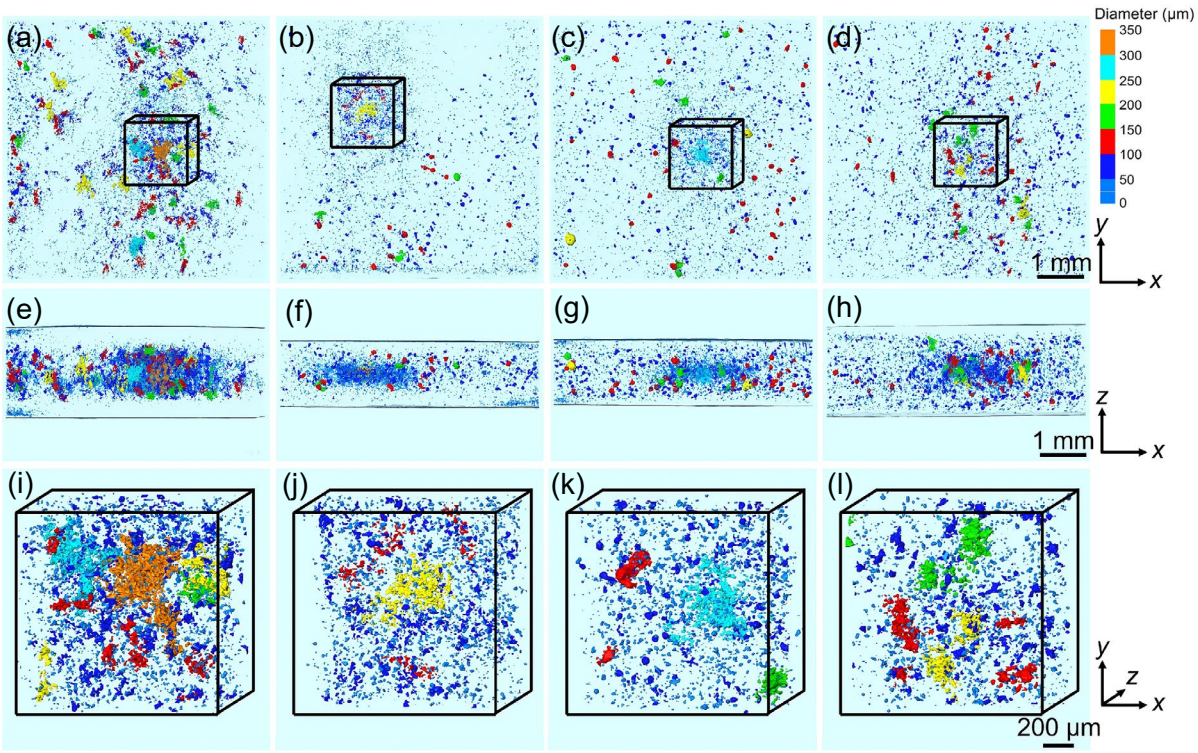

Fig. 5: Pore distribution at different sampling positions of battery module end: (a), (e), (i) Sample 1; (b), (f), (j) Sample 2; (c), (g), (k) Sample 3; and (d), (h), (l) Sample 4

Figure 6 presents the distribution of pore sphericity at different sampling locations on the HPDC AE81 magnesium alloy battery end plate. The sphericity values at all four locations predominantly range between 0.1 and 1. Among them, Sample 1 exhibits a higher frequency of pores with sphericity less than 0.5 and diameter greater than 50 μm, suggesting a predominance of net-shrinkage defects which may significantly compromise mechanical properties. Samples 2 to 4 show a higher proportion of pores with sphericity greater than 0.5 and diameter also larger than 50 μm, indicative of gas shrinkage pores. Gas shrinkage pores typically exhibit higher sphericity than net-shrinkage, displaying more rounded morphologies and potentially reducing stress concentration effects.

3.3 Mechanical properties

Figure 7 presents the room temperature mechanical properties of the battery end plate at different sampling locations. Specifically, Fig. 7(a) shows the representative stress-strain curves of specimens taken from different locations, while Fig. 7(b) presents the mean values and standard deviations of the tensile properties at room temperature. For Sample 1, the UTS, YS, and EL are measured as 218 MPa, 164 MPa, and 4.3%, respectively. From Samples 2 to 4, the YS values are 172 MPa, 175 MPa, and 178 MPa, respectively, indicating a slight increase, which is consistent with the previously observed grain refinement trend. Notably, the UTS at these samples rises by approximately 20 MPa compared to Sample 1, while EL improves by 2%–3%. The optimal performance is observed at Sample 4, with an UTS of 242 MPa, a YS of 178 MPa, and an EL of 6.8%.

With the increase in flow length, the mechanical properties of the alloy gradually improve; however, in large castings, maintaining thermal balance of the mold becomes highly challenging, often leading to shrinkage defects and a deterioration of mechanical properties in the latter-filled regions[19]. This tendency was not identified in the current investigation, likely due to the comparatively small dimensions of the casting.

These results demonstrate that the battery end plate possesses excellent room-temperature mechanical properties, fulfilling the industrial requirements for automotive battery pack applications.

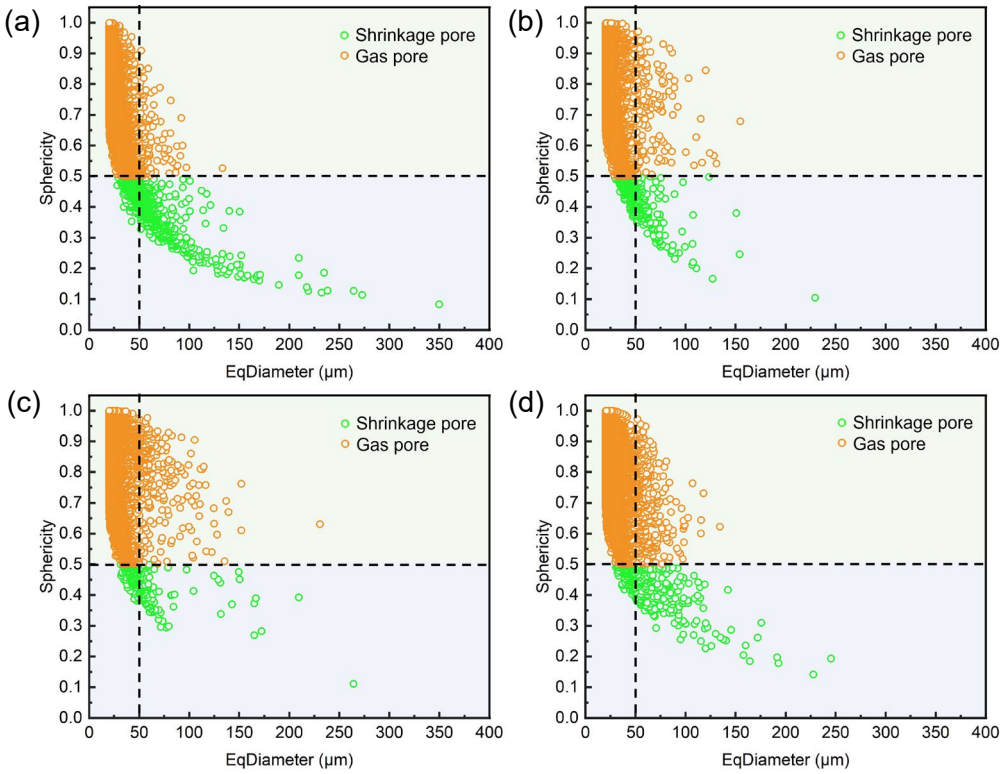

Fig. 6: Statistical analysis of pore sphericity at different sampling positions of the battery module end: (a) Sample 1; (b) Sample 2; (c) Sample 3; and (d) Sample 4

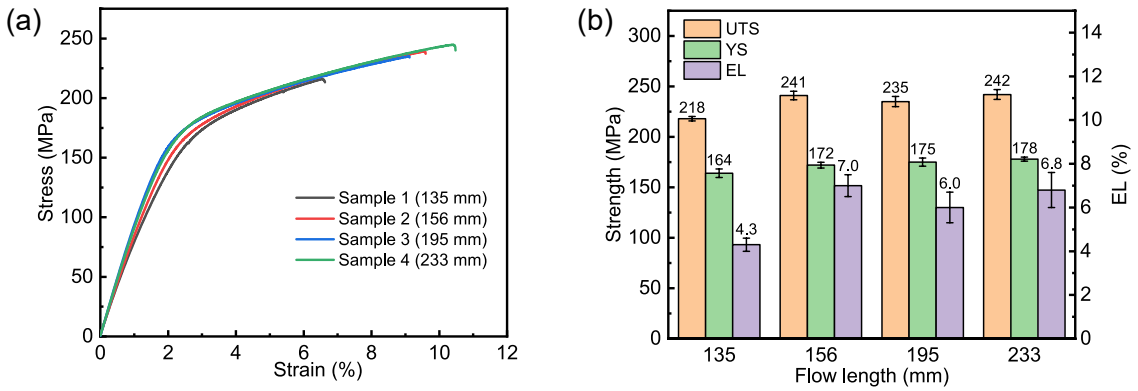

Fig. 7: Representative stress-strain curves of specimens taken from different locations (a) and mean values and standard deviations of tensile properties at room temperature (b)

3.4 Fracture morphology

To further investigate the fracture mechanisms under room temperature tensile conditions at different sampling positions, the fracture morphologies were characterized, as shown in Fig. 8. The locally enlarged images reveal distinct fracture features across the positions. At Sample 1, the presence of numerous pores and cleavage planes suggests a brittle cleavage fracture mechanism [Figs. 8(a–d)]. In contrast, Sample 2 exhibits a mixed ductile-brittle fracture mechanism, characterized by dimples, tear ridges, and a few cleavage planes [Figs. 8(e–h)]. Sample 3 displays features typical of brittle fracture, including pores and cleavage facets, alongside tear ridges and dimples, indicating a ductile-brittle mixed mode [Figs. 8(i–l)]. Similarly, Sample 4 shows a ductile-brittle mixed-mode fracture characterized by fewer pores and cleavage facets but more dimples and tear ridges, resembling the fracture morphology at Sample 2 [Figs. 8(m–p)], which also indicates a ductile-brittle mixed-mode fracture. Overall, the fracture morphology features align with the observed mechanical properties.

3.5 Influence of filling and solidification behavior on microstructure

The microstructure and mechanical properties of the HPDC AE81 magnesium alloy battery module end exhibit spatial variations. The alloy's microstructure formation is strongly influenced by melt filling dynamics, solidification behavior, and casting structural characteristics during the HPDC process[19, 20]. To elucidate the microstructure formation mechanisms across different regions and their correlation with mechanical performance, a systematic analysis of the filling and solidification behavior was conducted (Fig. 9). At 34.8% filling, the melt enters the inner gate, maintaining overall process stability. By 40.4% filling, the molten metal flows into

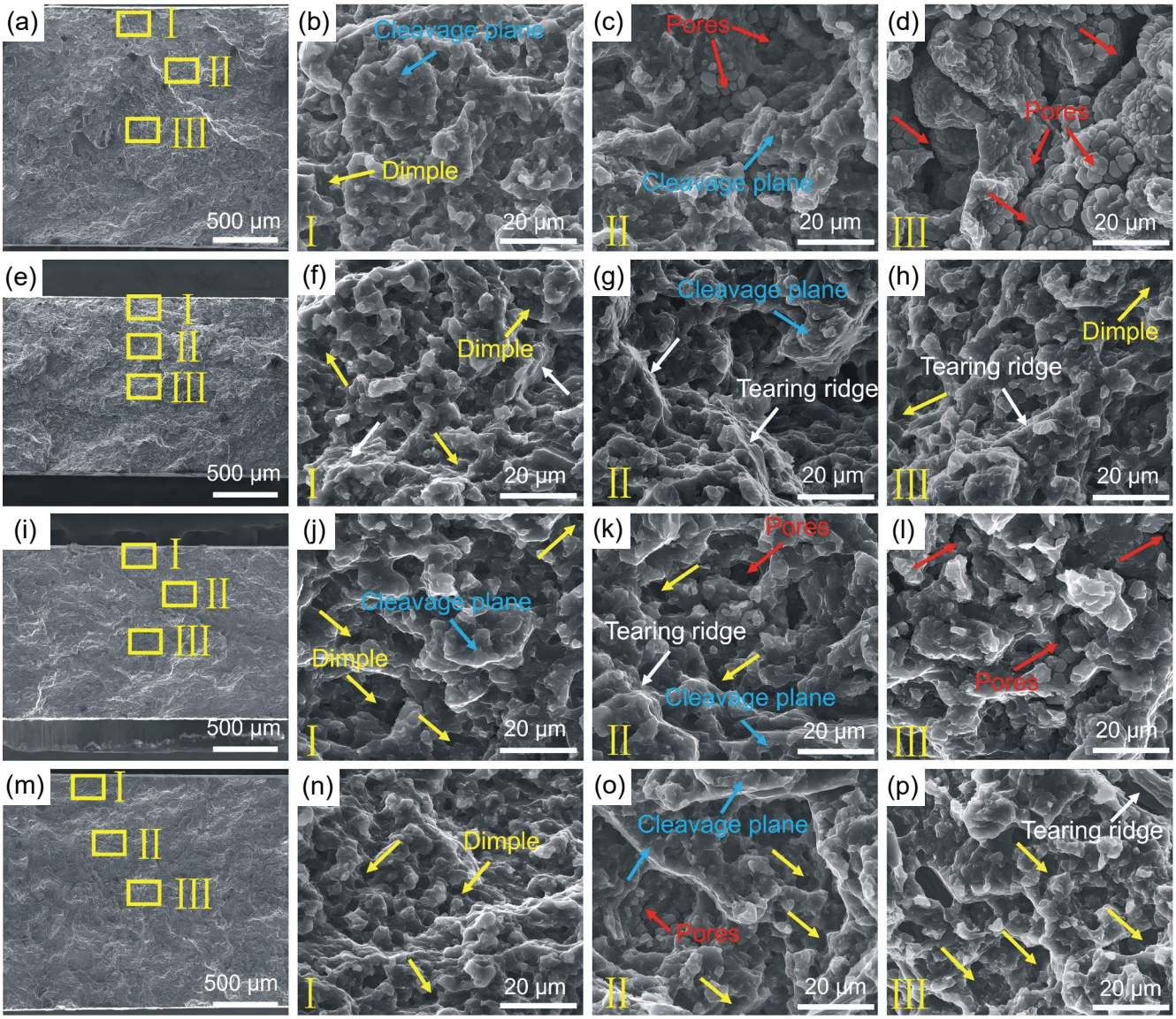

Fig. 8: Fracture surface morphologies at different sampling positions of the battery module end: (a–d) Sample 1; (e–h) Sample 2; (i–l) Sample 3; and (m–p) Sample 4

the casting cavity, forming partially hollow regions indicative of potential air entrapment. At 53.9% filling, the melt reaches Sample 3, though the bottom regions on both sides remain unfilled. Upon reaching 70.2% filling, the Sample 4 is fully filled, but air entrapment may persist at the lower sides of the casting. In summary, the HPDC AE81magnesium alloy exhibits a generally stable filling process, with localized air entrapment confined to specific areas.

In addition, the solidification sequence was examined by analyzing the evolution of solid fraction distribution through simulation during the solidification process (Fig. 10). Simulation results reveal that Samples 2 and 3 solidify more rapidly than Sample 1. This phenomenon is attributed to the 1.5 mm thin-walled structure at Samples 2 and 3, resulting in faster cooling and shorter solidification duration. Consequently, the reduced time for grain growth leads to smaller grain sizes. As a result, the mechanical properties at Samples 2 and 3 are superior to those at Sample 1. Simulation also shows that the solidification time at Sample 4 is similar to that at Sample 1. However, Sample 1 is situated closer to the biscuit and gate, where the melt temperature remains higher, potentially leading to grain coarsening. Thus, the comparatively finer average grain size at Sample 4 enhances its mechanical performance relative to Sample 1.

3.6 Effect of die-casting defects on mechanical properties

The multistage process in HPDC, comprising the slow shot, fast shot, and intensification pressure stages, promotes heterogeneous nucleation within the shot chamber, leading to the formation of primary grains and typical ESCs. Furthermore, unavoidable air entrapment and insufficient feeding during HPDC contribute to pore defects, both of which substantially impair the alloy's room-temperature mechanical properties. According to Wang and Zheng[41, 42], the tensile strength and ductility of HPDC alloys are closely linked to the ESCs' area fraction and size, lower ESCs content usually leads to better mechanical properties. In this study, the area fraction and average grain size of ESCs were measured at multiple locations on the AE81 HPDC battery module end (Fig. 11). The ESCs

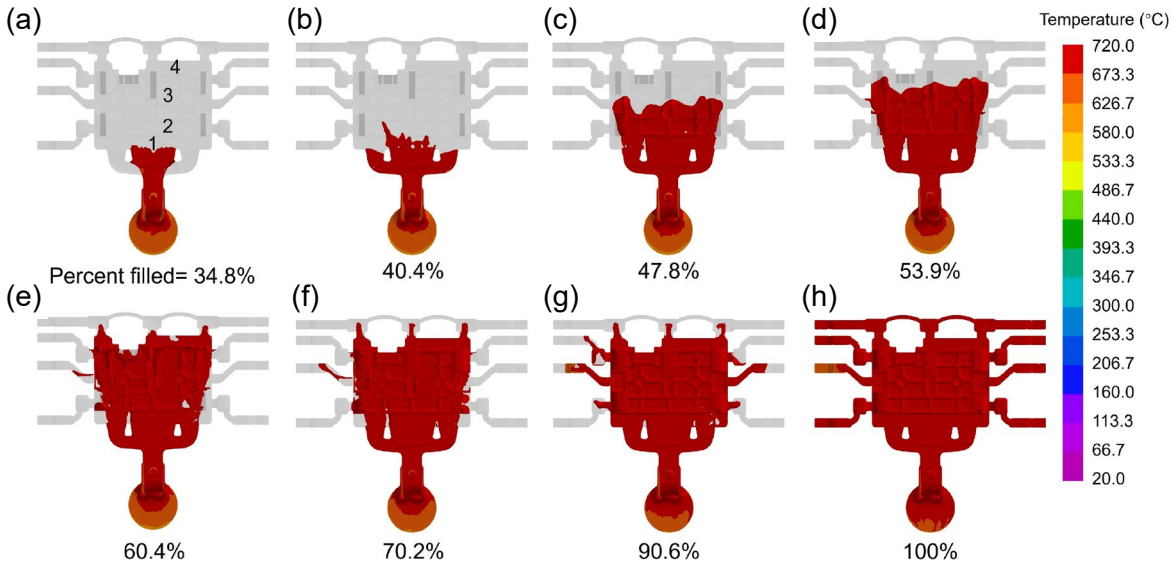

Fig. 9: Simulation results of mold-filling process of HPDC AE81 magnesium alloy battery module end component (a–h)

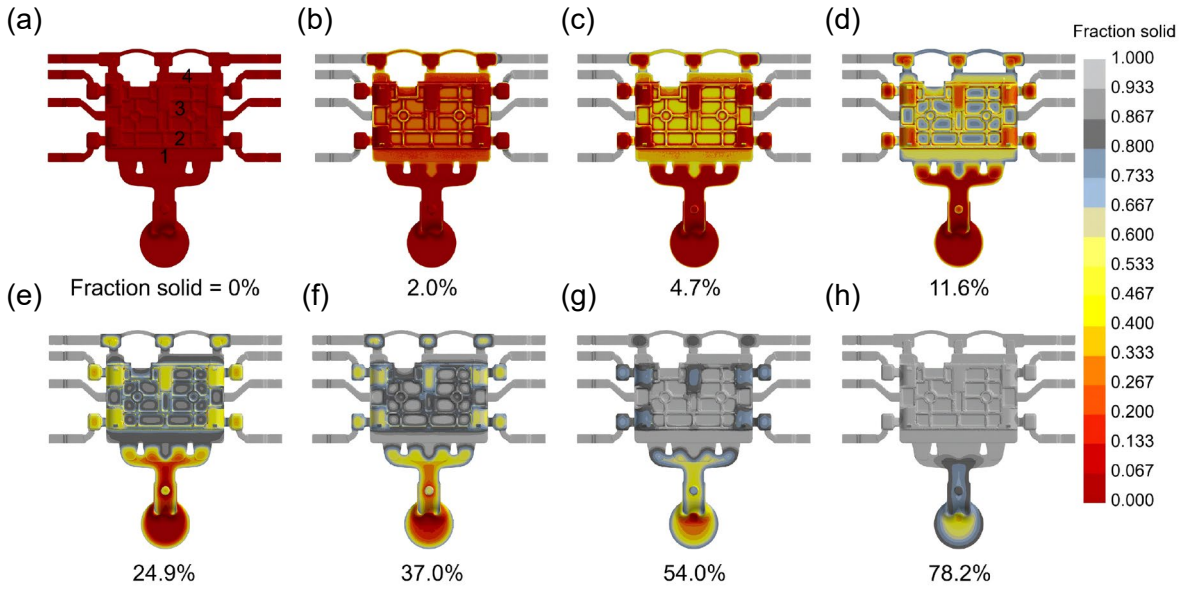

Fig. 10: Simulation results of solid fraction evolution during solidification of HPDC AE81 magnesium alloy battery module end component (a–h)

area fraction at Sample 1 is 53.09%, whereas it markedly decreases to 34.68% at Sample 4. This reduction can be attributed to the high-speed filling process, wherein the short flow path and intricate geometry of the battery module end subject the melt to intense shear forces, extensively fragmenting ESCs dendrites and significantly reducing their area fraction. Similarly, grain sizes at Samples 2 and 3 are smaller than at Sample 1, primarily due to lower ESCs content and faster solidification rates, as supported by simulation results showing shorter solidification times at these locations. Conversely, the grain size of ESCs at Sample 4 is larger than that at Samples 2 and 3, likely due to slower solidification, allowing ESCs grains more time to coarsen.

Numerous studies have demonstrated that porosity, as a critical microstructural feature of HPDC magnesium alloys, plays a decisive role in determining their room-temperature mechanical properties[15, 43]. As shown in Fig. 12, Sample 1 exhibits a pore volume fraction of 0.74%, which is approximately 2.2 times higher than those of Samples 2–4 (0.33%, 0.39%, and 0.34%). This substantial variation in porosity directly induces a gradient in mechanical performance. The elevated porosity at Sample 1 leads to diminished EL, YS, and UTS, while the lower porosity at Samples 2–4 corresponds to superior mechanical properties. That is, pores act as stress concentrators, substantially reducing the effective load-bearing cross-section and facilitating crack initiation, thereby deteriorating mechanical performance. Notably, despite comparable porosity levels among Samples 2–4, slight variations in mechanical behavior suggest that pore size, morphology, and spatial distribution also exert a considerable influence.

Studies have demonstrated that the fracture behavior of HPDC magnesium alloys at room temperature is strongly influenced by pore size, with cracks preferentially initiating at the largest pore defects[14, 40, 44]. As shown in Fig. 13, 3D

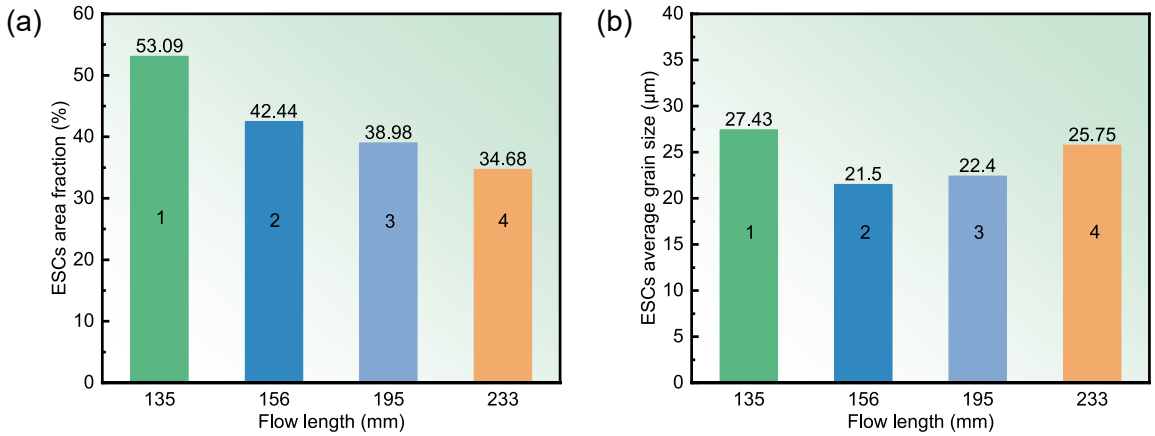

Fig. 11: Statistical results of ESCs area fraction (a) and average grain size (b) at different sampling positions (Samples 1 to 4) on the battery module end

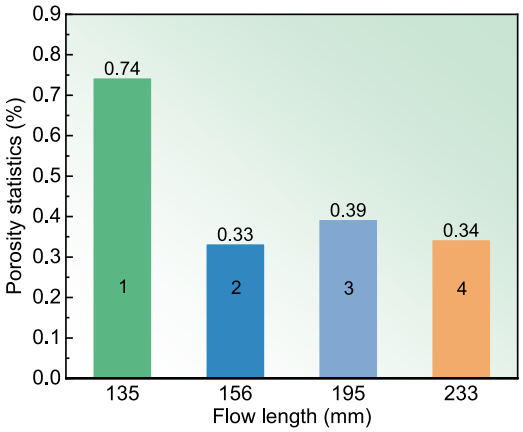

Fig. 12: Quantitative analysis of pore volume fractions at various sampling locations (Samples 1 to 4) of the battery module end

morphological analysis reveals significant variations in the largest pore characteristics at different locations of the battery module end. The pore in Sample 1 exhibits the largest equivalent diameter (349.92 μm) and the lowest sphericity (0.08), whereas Samples 2, 3, and 4 display maximum pore parameters of (229.57 μm, 0.18), (264.12 μm, 0.11), and (245.45 μm, 0.19), respectively. These geometric discrepancies result in notable mechanical performance differences: larger and less spherical pores induce more pronounced stress concentrations, leading to the poorest mechanical properties in Sample 1. In contrast, the other samples, characterized by smaller pore sizes and higher sphericity, exhibit superior mechanical performance. These findings underscore the critical role of pore morphology, particularly equivalent diameter and sphericity, in determining the mechanical properties of HPDC magnesium alloys.

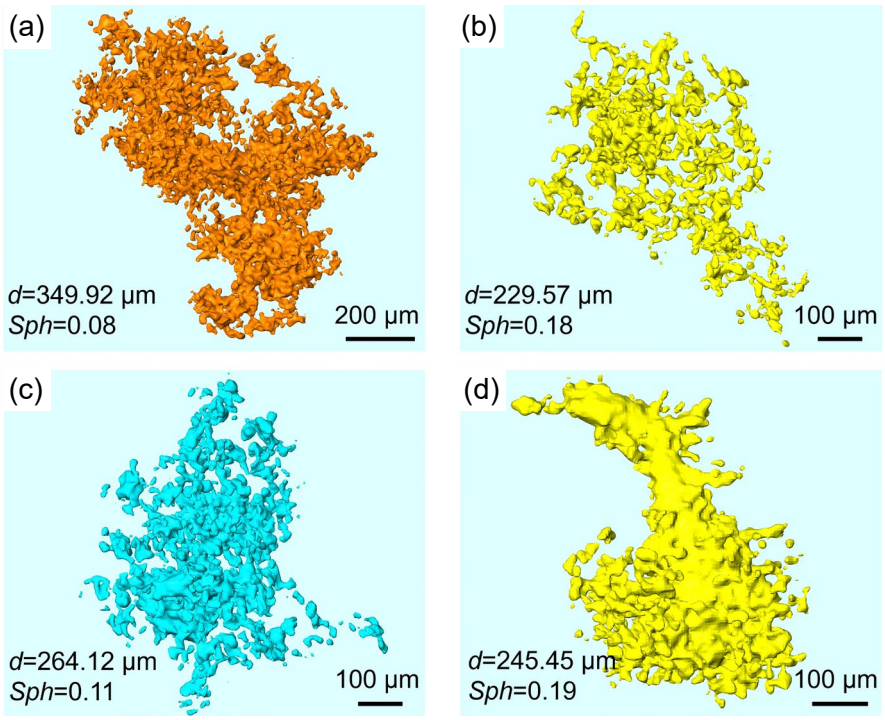

Fig. 13: 3D morphology of the largest pores at different sampling locations on the battery module end: (a) Sample 1; (b) Sample 2; (c) Sample 3; and (d) Sample 4

4 Conclusions

In this work, thin-walled AE81 magnesium alloy battery module ends were successfully fabricated via HPDC. A combined simulation and experimental approach was employed to investigate the effects of HPDC filling behavior and solidification sequence on the microstructure and mechanical properties of different regions within the cast components. The main conclusions are as follows:

(1) From the gate to the far end of the casting, the average grain size decreases from 16.54 μm at Sample 1 to 11.34 μm at Sample 4. Concurrently, the area fraction of externally solidified crystals reduces from 53.09% to 34.68%, contributing to a rise in yield strength from 164 MPa to 178 MPa.

(2) The elongation and ultimate tensile strength at different sampling positions vary significantly with the pore volume fraction. At Sample 1, the porosity reaches 0.74%, resulting in the lowest elongation (4.3%) and ultimate tensile strength (218 MPa). In contrast, at regions with lower porosities (0.33%–0.39%), elongation increases to 6%–7%, and ultimate tensile strength reaches 235–242 MPa.

(3) The performance of high-pressure die-cast AE81 magnesium alloy battery end plates improves with increasing flow length, which differs from the performance trend of large castings, possibly due to the relatively small size of the components. The mechanical properties, in particular, are strongly associated with grain size, ESCs area fraction, and porosity.

Acknowledgments

This work was financially supported by the National Key Research and Development Program of China (Grant Nos. 2022YFB3709300, 2021YFB3701000), the National Natural Science Foundation of China (Grant Nos. 52271090, 52071036, U2037601, U21A2048), the Chongqing Science and Technology Commission, China (Grant Nos. CSTB2022TIAD-KPX0021, CSTC2024YCJH-BGZXM0164, CSTB2024TIAD-KPX0001), and the Fundamental Research Funds for the Central Universities (Grant Nos. SKLMT-ZZKT-2022Z01, SKLMT-ZZKT-2022M12, 2022CDJDX-002, 2025CDJZKPT-05). We appreciate eceshi (www.eceshi.com) for the ICP analysis.

Conflict of interest

The authors declare that they have no known competing financial interests or personal relationships that could have appeared to influence the work reported in this paper.

References

[1] Gjestland H, Westengen H. Advancements in high pressure die casting of magnesium. Advanced Engineering Materials, 2007, 9(9): 769–776.
[2] Li T, Song J F, Zhang A, et al. Progress and prospects in Mg-alloy super-sized high pressure die casting for automotive structural components. Journal of Magnesium and Alloys, 2023, 11(11): 4166–4180.
[3] Xie H C, Zhao H, Guo X, et al. Recent progress on cast magnesium alloy and components. Journal of Materials Science, 2024, 59: 9969–10002.
[4] Song J F, Chen J, Xiong X M, et al. Research advances of magnesium and magnesium alloys worldwide in 2021. Journal of Magnesium and Alloys, 2022, 10(4): 863–898.
[5] Cam G, Günen A. Challenges and opportunities in the production of magnesium parts by directed energy deposition processes. Journal of Magnesium and Alloys, 2024, 12(5): 1663–1686.
[6] Wang Q H, Huang Z Q, Zhu Y C, et al. Study of corrosion behavior of Mg-Gd based soluble magnesium alloys. Metals, 2025, 15(1): 35.
[7] Zhu Y C, Wang N L, Chu Z B, et al. Study of the corrosion mechanism of Mg-Gd based soluble magnesium alloys with different initial texture states. Corrosion Reviews, 2023, 41(6): 659–672.
[8] Zhu Y C, Hao C R, Li Z L, et al. First-principles study of binary and ternary phases in Mg-Gd-Ni alloys. Physica: B, 2024, 685: 416065.
[9] Zhu Y C, Wang Q H, Huang Z Q, et al. Strain hardening exponent and strain rate sensitivity exponent of cast AZ31B magnesium alloy. Metals, 2022, 12(11): 1942.
[10] Zou J F, Ma L F, Zhu Y C, et al. Gradient microstructure and superior strength-ductility synergy of AZ61 magnesium alloy bars processed by radial forging with different deformation temperatures. Journal of Materials Science & Technology, 2024, 170: 65–77.
[11] Su C Y, Li D J, Wang J, et al. Enhanced ductility in high-pressure die casting Mg-4Ce-*x*Al-0.5Mn alloys via modifying second phase. Materials Science and Engineering: A, 2020, 773: 138870.
[12] Wang G G, Weiler J P. Recent developments in high-pressure die-cast magnesium alloys for automotive and future applications. Journal of Magnesium and Alloys, 2023, 11(1): 78–87.
[13] Chadha G, Allison J E, Jones J W. The role of microstructure on ductility of die-cast AM50 and AM60 magnesium alloys. Metallurgical and Materials Transactions: A, 2007, 38: 286–297.
[14] Zhang Y F, Zheng J, Xia Y T, et al. Porosity quantification for ductility prediction in high pressure die casting AM60 alloy using 3D X-ray tomography. Materials Science and Engineering: A, 2020, 772: 138781.
[15] Li X, Xiong S M, Guo Z. Improved mechanical properties in vacuum-assist high-pressure die casting of AZ91D alloy. Journal of Materials Processing Technology, 2016, 231: 1–7.
[16] Xie H C, Wang J, Li Y F, et al. Fast shot speed induced microstructure and mechanical property evolution of high pressure die casting Mg-Al-Zn-RE alloys. Journal of Materials Processing Technology, 2024, 331: 118523.
[17] Qin X Y, Su Y, Chen J, et al. Finite element analysis for die casting parameters in high-pressure die casting process. China Foundry, 2019, 16(4): 272–276.
[18] Dou K, Lordan E, Zhang Y J, et al. A complete computer aided engineering (CAE) modelling and optimization of high pressure die casting (HPDC) process. Journal of Manufacturing Processes, 2020, 60: 435–446.
[19] Niu Z C, Liu G Y, Li T, et al. Effect of high pressure die casting on the castability, defects and mechanical properties of aluminium alloys in extra-large thin-wall castings. Journal of Materials Processing Technology, 2022, 303: 117525.
[20] Gunasegaram D R, Givord M, O'Donnell R G, et al. Improvements engineered in UTS and elongation of aluminum alloy high pressure die castings through the alteration of runner geometry and plunger velocity. Materials Science and Engineering: A, 2013, 559: 276–286.

[21] Yang J, Liu B, Shu D W, et al. Effect of ultra vacuum assisted high pressure die casting on the mechanical properties of Al-Si-Mn-Mg alloy. Journal of Alloys and Compounds, 2025, 1026: 180531.
[22] Huang M J, Jiang J F, Wang Y, et al. Correlation between microstructures and mechanical properties of super-sized new-energy automobile structural component formed by vacuum HPDC process. Journal of Materials Research and Technology, 2025, 36: 1146–1159.
[23] Qin L, Porfyrakis K, Tzanakis I, et al. Multiscale interactions of liquid, bubbles and solid phases in ultrasonic fields revealed by multiphysics modelling and ultrafast X-ray imaging. Ultrasonics Sonochemistry, 2022, 89: 106158.
[24] Xiang K, Qin L, Zhao Y L, et al. Operando study of the dynamic evolution of multiple Fe-rich intermetallics of an Al recycled alloy in solidification by synchrotron X-ray and machine learning. Acta Materialia, 2024, 279: 120267.
[25] Qin L, Du W J, Cipiccia S, et al. Synchrotron X-ray operando study and multiphysics modelling of the solidification dynamics of intermetallic phases under electromagnetic pulses. Acta Materialia, 2024, 265: 119593.
[26] Zhang Z G, Khong J C, Koe B, et al. Multiscale characterization of the 3D network structure of metal carbides in a Ni superalloy by synchrotron X-ray microtomography and ptychography. Scripta Materialia, 2021, 193: 71–76.
[27] Huang S, Luo S F, Qin L, et al. 3D local atomic structure evolution in a solidifying Al-0.4Sc dilute alloy melt revealed in operando by synchrotron X-ray total scattering and modelling. Scripta Materialia, 2022, 211: 114484.
[28] Qin L, Zhang Z G, Guo B S, et al. Determining the critical fracture stress of al dendrites near the melting point via synchrotron X-ray imaging. Acta Metallurgica Sinica (English Letters), 2023, 36(5): 857–864.
[29] Wang X L, Zhao H D, Xu Q Y, et al. Tensile damage and fracture of high vacuum die-cast AlSiMgMn alloys with in-situ X-ray microtomography. Materials Science and Engineering: A, 2025, 924: 147869.
[30] Qin L, Maciejewska B M, Subroto T, et al. Ultrafast synchrotron X-ray imaging and multiphysics modelling of liquid phase fatigue exfoliation of graphite under ultrasound. Carbon, 2022, 186: 227–237.
[31] Hu C Y, Zhu H Y, Wang Y H, et al. Microstructure features and mechanical properties of non-heat treated HPDC Al9Si0.6Mn-TiB_2 alloys. Journal of Materials Research and Technology, 2023, 27: 2117–2131.
[32] Zhu S M, Gibson M A, Nie J F, et al. Microstructural analysis of the creep resistance of die-cast Mg-4Al-2RE alloy. Scripta Materialia, 2008, 58(6): 477–480.
[33] Yang Q, Lv S H, Meng F Z, et al. Detailed structures and formation mechanisms of well-known $Al_{10}RE_2Mn_7$ phase in die-cast Mg-4Al-4RE-0.3Mn alloy. Acta Metallurgica Sinica (English Letters), 2019, 32: 178–186.
[34] Xie H C, Li Y F, Song J F, et al. Effect of intensification casting pressure on microstructure and mechanical properties of high pressure die casting AE81 magnesium alloy. Journal of Materials Research and Technology, 2025, 36: 10092–10103.
[35] Nemcko M J, Wilkinson D S. On the damage and fracture of commercially pure magnesium using x-ray microtomography. Materials Science and Engineering: A, 2016, 676: 146–155.
[36] Li X, Xiong S M, Guo Z. Correlation between porosity and fracture mechanism in high pressure die casting of AM60B alloy. Journal of Materials Science & Technology, 2016, 32(1): 54–61.
[37] Zhang T T, Yu W B, Ma C S, et al. The effect of different high pressure die casting parameters on 3D microstructure and mechanical properties of AE44 magnesium alloy. Journal of Magnesium and Alloys, 2022, 11(9): 3141–3150.
[38] Yu W B, Ma C S, Ma Y H, et al. Correlation of 3D defect-band morphologies and mechanical properties in high pressure die casting magnesium alloy. Journal of Materials Processing Technology, 2021, 288: 116853.
[39] Weiler J P, Wood J T, Klassen R J, et al. Relationship between internal porosity and fracture strength of die-cast magnesium AM60B alloy. Materials Science and Engineering: A, 2005, 395(1): 315–322.
[40] Song J, Xiong S M, Li M, et al. The correlation between microstructure and mechanical properties of high-pressure die-cast AM50 alloy. Journal of Alloys and Compounds, 2009, 477(1): 863–869.
[41] Wang Q L, Xiong S M. Effect of multi-step slow shot speed on microstructure of vacuum die cast AZ91D magnesium alloy. Transactions of Nonferrous Metals Society of China, 2015, 25(2): 375–80.
[42] Zheng H T, Jiang Y H, Liu F, et al. Microstructure heterogeneity optimization of HPDC Al-Si-Mg-Cu alloys by modifying the characteristic of externally solidified crystals. Journal of Alloys and Compounds, 2024, 976: 173167.
[43] Dong X X, Zhu X Z, Ji S X. Effect of super vacuum assisted high pressure die casting on the repeatability of mechanical properties of Al-Si-Mg-Mn die-cast alloys. Journal of Materials Processing Technology, 2019, 266: 105–113.
[44] Zhang Y F, Zheng J, Shen F H, et al. Analysis of local stress/strain fields in an HPDC AM60 plate containing pores with various characteristics. Engineering Failure Analysis, 2021, 127: 105503.